JOURNAL OF GEOPHYSICAL RESEARCH, VOL. 105, NO. C9, PAGES 22,015–22,033, SEPTEMBER 15, 2000

Estimation of wave phase speed and nearshore bathymetry from video imagery

Hilary F. Stockdon[1] and Rob A. Holman

College of Oceanic and Atmospheric Sciences, Oregon State University, Corvallis

Abstract. A new remote sensing technique based on video image processing has been developed for the estimation of nearshore bathymetry. The shoreward propagation of waves is measured using pixel intensity time series collected at a cross-shore array of locations using remotely operated video cameras. The incident band is identified, and the cross-spectral matrix is calculated for this band. The cross-shore component of wavenumber is found as the gradient in phase of the first complex empirical orthogonal function of this matrix. Water depth is then inferred from linear wave theory's dispersion relationship. Full bathymetry maps may be measured by collecting data in a large array composed of both cross-shore and longshore lines. Data are collected hourly throughout the day, and a stable, daily estimate of bathymetry is calculated from the median of the hourly estimates. The technique was tested using 30 days of hourly data collected at the SandyDuck experiment in Duck, North Carolina, in October 1997. Errors calculated as the difference between estimated depth and ground truth data show a mean bias of -35 cm (rms error = 91 cm). Expressed as a fraction of the true water depth, the mean percent error was 13% (rms error = 34%). Excluding the region of known wave nonlinearities over the bar crest, the accuracy of the technique improved, and the mean (rms) error was -20 cm (75 cm). Additionally, under low-amplitude swells (wave height $H \leq 1$ m), the performance of the technique across the entire profile improved to 6% (29%) of the true water depth with a mean (rms) error of -12 cm (71 cm).

1. Introduction

The nearshore zone is the energetic region of the coastal environment where ocean waves shoal and interact with local morphology. It is an area of dramatic and rapid change as seen by our ever-varying eroding and accreting shorelines. Changes in bathymetry can occur on time scales as short as hours to days (such as in the presence of large storm and infragravity waves) and on spatial scales of the order of meters to kilometers. Problems associated with coastal erosion impacts coupled with increased development along the oceans have created a strong need for knowledge of how this complex system behaves.

The dynamics of nearshore processes are determined by two components: the fluid motions and the resulting sediment response. The beach profile forms the bottom boundary condition for all fluid motions in the nearshore and is directly or indirectly responsible for all evolutions of the wave field. For example, the shoaling profile causes waves to steepen and eventually break, moving energy into higher frequencies and turbulence in a way that depends on the nature of the beach profile. Gradients in wave momentum (radiation stress) associated with breaking can drive mean longshore and cross-shore currents and setup [*Longuet-Higgins,* 1970]. On more complex topographies, rips currents may occur over discontinuities or breaks in the offshore bar. Edge waves may develop and become trapped on the beach [*Holman and Bowen,* 1979] or over offshore sand bars, concentrating energy along the bar rather than along the shore [*Bryan and Bowen,* 1996].

The nature of the beach profile is also a response to the overlying fluid forcing. The overall steepness of the beach has been related to the offshore wave steepness [*Shepard,* 1950] with erosion and flattening during storms and steepening during intervening calm periods. The generation and evolution of sand bars have been associated with either the break point of incident waves [*Sallenger and Howd,* 1989] or the motion of infragravity edge waves [*Bowen and Inman,* 1971].

A common result of the strong feedback between the forcing and response components of the nearshore system is complex morphologies. For example, *Wright and*

[1]Now at Center for Coastal Geology, U.S. Geological Survey, St. Petersburg, Florida

Paper number 1999JC000124.
0148-0227/00/1999JC000124$09.00

Short [1984] introduced a detailed description of beach morphology which required six beach states to describe the variability of a set of Australian beaches. *Lippmann and Holman* [1990] found general agreement by applying a slightly modified classification scheme to 2 years of time exposure images, 10-min averages of breaking patterns which allow for visualization of sand bar morphology. However, extension of the approach to the subsequent 3 years was unsuccessful due to large interannual changes in the observed nearshore morphology.

Thus bathymetry data are important not only for their own sake, as a record of the changing beach, but also as a key component for understanding the overlying fluid dynamics and the interactions between fluid motions and bathymetry. Collection of large-scale, long-term data sets of bathymetry is a high-priority requirement for the advancement of nearshore science.

1.1. Collection of Bathymetric Data

Historically, the collection of offshore bathymetric profiles has been a costly and labor-intensive task. Traditionally, bathymetric surveys have been collected using a survey rod, sighting and recording the height of a target rod that must be held against the bottom by a diver. For deeper points the moving position of a small boat would be recorded from shore while onboard fathometer depths were recorded. The resulting data coverage was sparse and often of low accuracy owing to waves or surge contamination of vertical signals. Recent systems based on small boats equipped with accurate GPS systems have eliminated the vertical errors, but sampling will continue to remain sparse in time because of costs and logistical difficulty. Data are especially difficult to collect during periods of large waves or strong currents. However, these conditions often represent the most energetic periods of sediment transport and are the times of greatest scientific interest.

Estimation of nearshore depths from wave propagation characteristics is not a new idea. During World War II, scientists began to take a greater interest in studying wave propagation and phase speed in order to predict surf conditions and bathymetry for safe military landings [*Williams,* 1946]. In the late 1940s and 1950s the remote sensing technique for determining water depth was based on time-lapse aerial photography of the ocean surface. After measuring the distance that a wave had traveled relative to a baseline or a fixed point in the water and the time between successive images, wave speed was calculated, and water depth was inferred [*Johnson,* 1949; *Fuchs,* 1953]. Long-crested, high-amplitude waves were critical to accurate estimation of wave speed as the short-crested wind waves were felt to obscure clear identification of the dominant wave crests [*Wiegel and Fuchs,* 1953]. Determination of water depth from wave speed has been considered more recently by several authors for application to other remote sensing platforms such as synthetic aperture radar (SAR) [*Greidanus,* 1997], X band radar [*Bell,* 1999], and SPOT (satellite) images [*Leu et al.,* 1999].

1.2. Potential for a Video-Based Technique

Here we present a technique that will allow for the regular, long-term automatic collection of bathymetry data using imagery collected from video cameras. First, wave celerity, or wave phase speed, is measured from remotely collected video intensity data, and then local water depth is inferred based on linear wave theory. The measurement of wave phase speed and associated water depths made at a series of cross-shore positions provides us with a cross-shore profile of beach morphology. These remotely collected profiles may create a long and complete record of the large-scale morphology changes at a particular site, in addition to providing depth data for testing of various nearshore process models. Incorporation of the technique into the automated sampling routine of the well-established Argus [*Aarninkhof and Holman,* 1999] will allow for a more comprehensive and long-term sampling of nearshore bathymetry, a prerequisite to the study of the large-scale behavior of profile response.

Video estimation of bathymetry is just one of a suite of recent techniques that have included detection and measurement of submerged sand bar systems [*Lippmann and Holman,* 1989], wave runup [*Holland and Holman,* 1999; *Holland et al.,* 1995], and foreshore beach slope measurement [*Plant and Holman,* 1997]. Remote sensing techniques offer an attractive tool for these measurements because they allow sampling over a large span of spatial (centimeters to kilometers) and temporal scales (seconds to years) [*Holland et al.,* 1997], do not involve the deployment of any instruments into the damaging environment of the surf zone, and allow creation or modification of spatial sampling arrays at any time.

Section 2 of this paper provides a general background on wave phase speed and on how video may be used to measure this quantity in the nearshore. In the section 3 the video technique for estimating bathymetry is discussed in detail. Section 4 presents the results of the video depth analysis from the SandyDuck experiment in Duck, North Carolina, in October 1997. Section 5 presents a discussion of the accuracy of the technique and of the conditions under which it can best be applied. Finally, a brief summary of the conclusions of this research is presented in section 6.

2. Theory

The phase speed, or celerity, c, of a wave is defined as the wavelength L divided by the wave period T or, equivalently,

$$c = \frac{\sigma}{k}, \tag{1}$$

where the wavenumber k is defined as $2\pi/L$ and the radial frequency σ is defined as $2\pi/T$.

Linear wave theory relates wavenumber and frequency through the dispersion equation,

$$\sigma^2 = gk \tan \mathrm{h}(kh), \tag{2}$$

where g is the acceleration of gravity and h is the local water depth [*Dean and Dalrymple,* 1991]. From (1) and (2) the celerity of a wave based on linear wave theory is

$$c = \frac{\sigma}{k} = \frac{g}{\sigma} \tan \mathrm{h}(kh). \tag{3}$$

Approximations to the exact solution exist for waves propagating in deep and shallow water. As water depth becomes large, $h/L_o > 0.5$, we can make the approximation $\tanh(kh) \sim 1$. Thus we can define a simple deep water wavelength L_o to be

$$L_o = \frac{gT^2}{2\pi}, \tag{4}$$

and the phase speed then becomes

$$c = \frac{g}{\sigma} = \frac{gT}{2\pi}. \tag{5}$$

In shallow water ($h/L_o < 0.05$), $\tanh(kh) \sim (kh)$, and the phase speed of a wave simplifies to

$$c^2 = \frac{\sigma^2}{k^2} = gh, \tag{6}$$

which is no longer dependent on the wave period but is solely a function of the depth of water through which the wave is propagating. Thus measurements of celerity, gathered by remote sensing, can be inverted using (6) or, more generally, (3) to yield estimates of local depth.

2.1. Measurement of Wave Phase Speed

There have been a number of studies that directly tested theoretical predictions of phase speed against field data. An early investigation used a photographic technique involving calibrated wave poles placed across the breaker zone to measure wave phase speed [*Suhayda and Pettigrew,* 1977]. The average wave crest speed was approximated by measuring the distance a particular wave crest had moved over the interval of time and then compared to solitary theory. Maximum discrepancies were observed at the breakpoint, where measured speeds were 20% greater than those predicted by solitary theory, and in the midsurf zone, where measured values were ~20% less than the predicted values. Errors in the calculation were attributed to problems in visually determining the crest of the wave and to the fact that the speed of the crest does not represent the speed of the wave as a whole. This study alluded to the benefits of data collection using continually recording wave staffs and set the stage for more advanced measuring techniques that would follow.

Eventually, wave phase speed calculations were made from continuous time series collected from wave staffs or pressure sensors. As a part of the Nearshore Sediment Transport Study, *Thornton and Guza* [1982] used pairs of wave gauges aligned perpendicular to the beach to obtain cross-spectral information on the frequency-dependent relative phase difference $\phi(f)$ between waves at the two sensor locations. The phase speed was then calculated as

$$c_x = \frac{2\pi f \Delta x}{\phi(f)}, \tag{7}$$

where c_x is the cross-shore component of phase speed and Δx is the spatial separation between sensors. Results showed agreement with linear theory, accurate to within 20 to -10% within the incident band, with some finite amplitude dispersion.

2.2. Video Techniques

The phase speed of a progressive wave may be similarly observed using video-based techniques since waves have a measurable visible signature. The observed relationship between the true wave signal and a remotely sensed video signal can be described by the modulation transfer function (MTF), $M(f)$, a linear spectral representation of the relative amplitudes and phases between an input signal $X(f)$ and an output signal $G(f)$ [*Gonzales and Woods,* 1992].

$$G(f) = M(f)X(f). \tag{8}$$

This complex gain function can be used to describe the relationship between both the phases and amplitudes of the visual signature of the waves and the true waveform. Techniques described in this paper will primarily be based on signal phases.

The nature of the MTF depends on the mechanism by which the waves are seen. Seaward of the breakpoint the sea surface is visible primarily because of specular (directional) reflection of downwelling sky radiance. Variations in sea surface slope due to waves cause reflection from different elevations in the sky, making the wave visible owing to the sky gradient (the variation of sky brightness from very bright near the horizon to darker near the zenith [*Lynch and Livingston,* 1995]). Thus the seaward face of the wave (away from a land-based camera) is usually light, while the landward, front face is dark. The angle of view relative to wave rays also determines how strong the visible signal will be. For example, if one were to look along a wave crest, there will be no sea surface slope component in the direction of view; therefore the wave would not be discernible.

In the region prior to wave breaking the phase of the MTF is relatively steady in space, only evolving significantly in the shoaling region near the breakpoint. Once waves begin to break, individual wave crests can be recognized by diffuse (scattered) reflection from the white foam associated with the turbulence of breaking. Since a white face now marks the signature of the wave rather than the darker faces observed outside of the break point, the MTF shows a different, yet still coherent, phase relationship between the remotely sensed signal and the true signal. Because the reflection is

diffuse, there is no longer any dependence on viewing geometry.

Lippmann and Holman [1991] carried out preliminary tests of the relationship between remotely sensed video data and the actual waveform by comparing time series of video intensity of a pixel (pixel intensity time series) to time series of pressure data from a collocated pressure sensor. Cross spectra between the video and pressure sensor data showed high coherence in the incident frequency band. Phase was spatially dependent on whether the waves were breaking. Thus, for applications such as phase progression of breaking waves, video may serve as a valid proxy for fixed instruments [*Lippmann and Holman,* 1991].

Lippmann and Holman [1991] further tested the capability of video data analysis for estimation of phase speed and wave angle of individual breaking waves using data from the 1990 Delilah experiment in Duck, North Carolina. Using pixel intensity time series collected with a 4-m-wide square array, phase speeds and wave angles were calculated. Celerites exceeded linear theory by up to 20%, suggesting some amplitude dispersion.

We wish to extend the individual point estimates of celerity found by *Lippmann and Holman* [1991] to allow full cross-shore coverage. This simply involves the extension of the pair-wise calculation to a full array of locations and then the estimation of wave phase speed along transects. Results may then be averaged over multiple data runs to yield statistically stable estimates of bathymetry.

3. Video Technique for Bathymetry Estimation

From (3) the local water depth at cross-shore position x can be found from

$$h(x) = \frac{\tanh^{-1}\left(\frac{\sigma^2}{gk(x)}\right)}{k(x)}. \tag{9}$$

The presence of the hyperbolic tangent in (9) makes the expression for depth complicated to solve. The shallow water expression for celerity may appear to provide an alternatively simple calculation of depth but will yield errors that increase with depth.

Figure 1 presents a comparison between the full dispersion relationship and the shallow water approximation. In Figure 1a, water depth is plotted versus the wavelength, with both quantities normalized by the

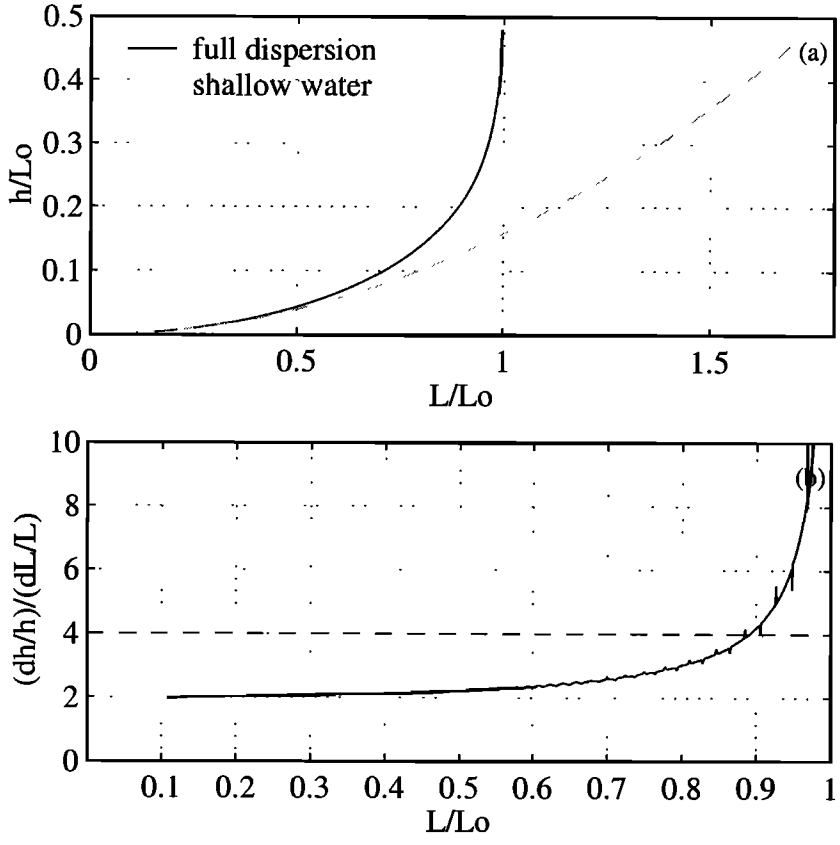

Figure 1. Sensitivity analysis of the dispersion relation based on deep water wavelength. (a) Plot of the linear dispersion relation, comparing wavelength to local water depth, both normalized by the deep water wavelength. The solid line corresponds to the full dispersion equation, while the dashed line represents the shallow water approximation. (b) The sensitivity of the predicted depth to errors in the estimated wavelength, both expressed as a percentage, versus relative wavelength. The dashed line at $y = 4$ indicates the cutoff value selected for this study.

deep water wavelength (only a function of wave period). The two curves begin to diverge visually at $L/L_o \sim 0.55$.

As L/L_o approaches 1, the ability to estimate water depth becomes very sensitive to errors in wavelength, and the technique becomes unusable. Figure 1b shows the relationship between the relative error in wavelength (dL/L) and the corresponding relative error in water depth (dh/h). For shallow water, errors in depth asymptotically approach a value twice the wavelength errors. For deeper water the sensitivity to errors steadily worsens, becoming infinite as L/Lo approaches 1. Values of the ratio of the relative errors for which the sensitivity exceeds 4 (corresponding to $L/L_o > 0.9$) were neglected.

Equation (9) can be expanded to allow for an oblique wave approach,

$$h(x) = \frac{\tanh^{-1}\left(\frac{\sigma^2}{gk(x)}\right)}{k(x)} = \frac{\tanh^{-1}\left(\frac{\sigma^2}{g\sqrt{k_x^2(x)^2+k_y^2(x)^2}}\right)}{\sqrt{k_x^2(x)^2+k_y^2(x)^2}}, \tag{10}$$

where $k_x(x)$ and $k_y(x)$ are the cross-shore and longshore components of wavenumber. The estimation of water depth is now reduced to the measurement of both wavenumber components and the incident frequency from pixel intensity data.

3.1. Estimation of Frequency

The video technique first involves the collection of pixel intensity time series at an array of pixel locations. A cross-shore timestack (space-time image, Figure 2) illustrates the variations in wave amplitude (or, for the video technique, pixel intensity) at each cross-shore location through time. The traces of wave crests can be used to estimate the speed of the shoreward, progressive waves.

The data set for analysis consists of pixel intensity time series from a single cross-shore and multiple alongshore arrays of pixel locations. The data are first smoothed with a high-pass filter to remove low-frequency trends (f <0.05 s^{-1}) and then again with a low-pass filter to remove noise (f >0.5 s^{-1}). Spectra are calculated at each cross-shore sensor location using a bandwidth of 0.0205 s^{-1} and 42 degrees of freedom. An average spectrum is then calculated over all cross-shore locations. The spectral peak is selected as the frequency corresponding to the center of mass, within a predefined incident frequency range of 0.05-0.20 s^{-1}, calculated as

$$f_{cm} = \frac{\sum_{i=1}^{N} S_i f_i}{\sum_{i=1}^{N} S_i}, \tag{11}$$

where N is the number of frequency bins. Only a narrow band of frequencies about the incident peak is considered since lower frequencies are often incoherent and higher frequencies are often just phase-locked harmonics of the fundamental whose celerity will not be that of a free wave.

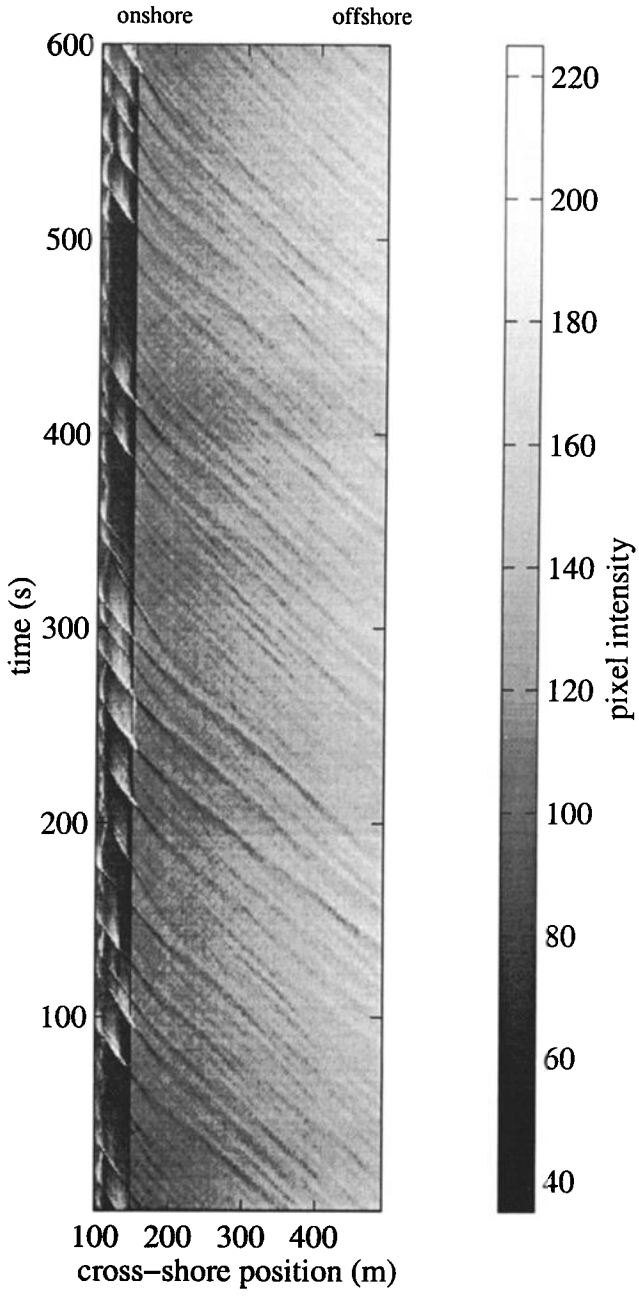

Figure 2. Intensity timestack from SandyDuck, Duck, North Carolina, October 14, 1997 at 0700 LT. Bright regions generally indicate wave breaking over shallow features. The slope of the wave traces can be used to compute the approximate speed of the shoreward progression of waves. The jump in intensity at x = 140 m marks the boundary between the two cameras (with different gains) and is removed in subsequent analysis.

3.2. Estimation of Cross-Shore Wavenumber

The cross-shore wavenumber is determined from analysis of wave phase structure using a frequency domain (complex) empirical orthogonal function (CEOF) of the data collected from the cross-shore array. The CEOF analysis is a method for detecting propagating signals from data collected over spatially separated sensors and

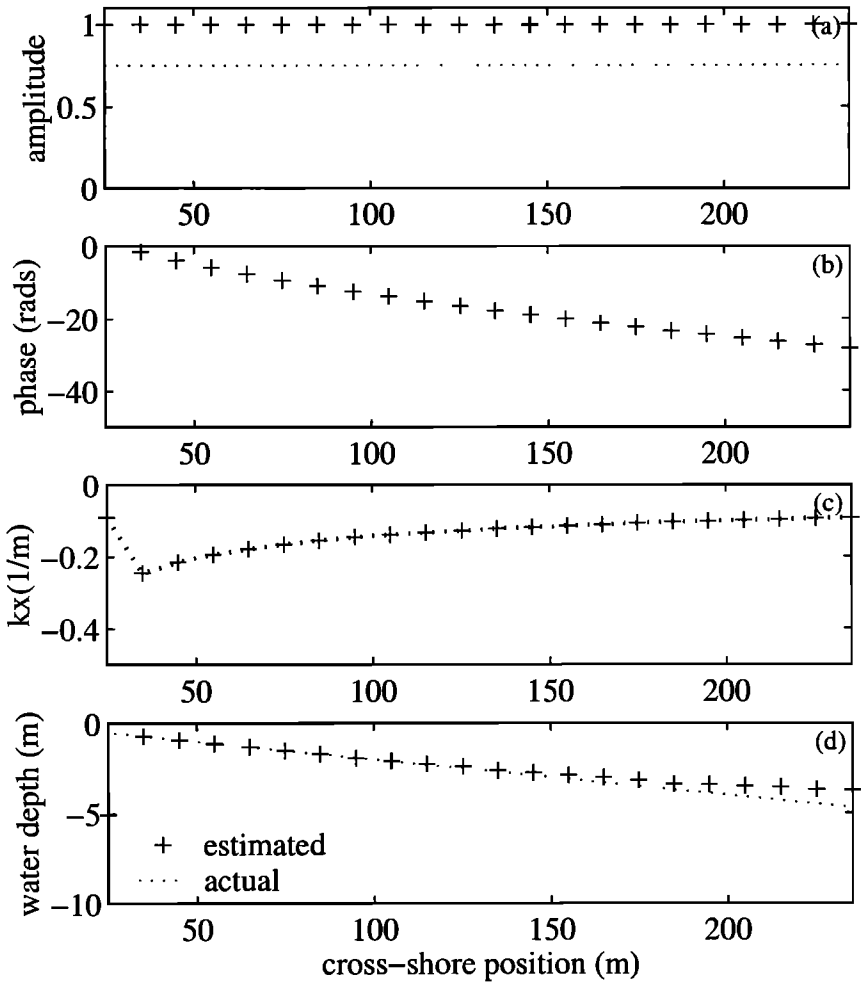

Figure 3. Synthetic series test for the extraction of cross-shore wavenumber. (a) Amplitude, (b) phase, (c) cross-shore wavenumber, and (d) estimated water depth are presented as a function of the cross-shore position. The amplitude structure shows that the first EOF explains ~100% of the variance uniformly across the profile. From the slope of the phase ramp the cross-shore wavenumber is calculated. Estimated depths are compared to the input depth profile.

involves eigenvector analysis of the cross-spectral matrix within a frequency band of interest. This type of analysis allows waves of different frequencies to be resolved and then defines their amplitudes and phases from the magnitude and phase of the first complex eigenvector [*Wallace and Dickinson,* 1972].

For the video technique the input signal is that of pixel intensity $I(x,t)$. The Fourier transform of the data is represented as

$$Y(x,f) = FT[I(x,t)]. \tag{12}$$

The cross-spectral matrix is then calculated as

$$Q_{ij}(f) = \langle Y_i^* Y_j \rangle, \tag{13}$$

where Y_i^* is the complex conjugate of the Fourier transform and angle brackets represent an ensemble averaging, here approximated by averaging over the frequencies within the band of interest. The cross spectrum is then normalized

$$Q' = \Omega^{1/2} Q \Omega^{1/2'} \tag{14}$$

by the diagonal matrix Ω, which contains the variance $\sigma^2(x_i)$ at each position. Eigenvector analysis of the normalized cross-spectral matrix yields a normalized eigenvector,

$$\Lambda(f) = EOF[Q(f)']. \tag{15}$$

The percent variance explained by the first mode of Λ can be expressed as

$$V_1 = \frac{\lambda_1}{\sum_{i=1}^{N} \lambda_i}, \tag{16}$$

where λ_i are the eigenvalues. The first mode generally contains the majority of the variability within the data set [*Merrifield and Guza,* 1990]. Therefore we select the first mode, complex eigenvector

$$\Lambda_1 = a(x) + ib(x), \tag{17}$$

as the single mode to represent the cross-shore struc-

ture. The phase ϕ and amplitude A at each cross-shore position can be calculated as

$$A(x) = \sqrt{(a^2(x) + b^2(x))}, \quad (18)$$

$$\phi(x) = \tan^{-1}\left(\frac{b(x)}{a(x)}\right). \quad (19)$$

Finally, wavenumber is calculated as the cross-shore gradient in phase [*Merrifield and Guza,* 1990]

$$k_x(x) = \frac{d\phi}{dx}. \quad (20)$$

For regions in which $A(x)$ is large the cross-shore phase structure of the mode is likely to be significant. Low amplitudes at the ends of the array and erratic fluctuations of amplitudes within the array are indications of a noisy signal and low coherence across the array [*Merrifield and Guza,* 1990]. To avoid spurious results, a threshold amplitude was arbitrarily chosen as 0.60, below which the EOF structure was considered to be unreliable.

The proposed technique for estimating cross-shore wavenumber was tested using a synthetic time series based on a shore-normal 10-s wave shoaling on a beach with a slope of 0.02. The amplitude structure (Figure 3a) shows that the first EOF explains ~100% of the variance uniformly across the beach. A phase ramp, shown to steepen onshore (Figure 3b), indicates a shoreward progressive wave whose phase speed decreases as it shoals. From the slope of this phase ramp the cross-shore wavenumber (Figure 3c) is calculated. Knowing the wave period of this test a priori (or, in the case on a natural beach, from the frequency selection previously described), the depth can then be estimated using (10) and compared to the input depth profile (Figure 3d). The close comparison between the two confirms the merit of the analysis approach.

3.3. Estimation of Longshore Wavenumber

On natural beaches, waves rarely approach from directly offshore. Therefore the longshore component of wavenumber k_y must be estimated. The longshore wavenumber is determined by performing a similar CEOF analysis of a set of longshore pixel arrays. The longshore wavenumber is calculated as the least squares fit over the full longshore array of the longshore gradient in phase ϕ associated with the first mode of the EOF

$$k_y(x) = \frac{d\phi}{dy}. \quad (21)$$

Knowledge of both the cross-shore and longshore components of wavenumber allows for the calculation of wave angle α at each point in the cross-shore array as

$$\alpha(x) = \tan^{-1}\left(\frac{k_y(x)}{k_x(x)}\right). \quad (22)$$

4. Field Test

The development and initial tests of the video technique were performed with data collected as a part of the SandyDuck experiment, conducted during September and October 1997 at the U.S. Army Corps of Engineers Field Research Facility (FRF) located in Duck, North Carolina. One data run from SandyDuck will be used to first illustrate the technique and explain initial results. The technique was then further tested using data collected from October 1–30 along 18 cross-shore transects.

The FRF site in Duck, North Carolina, is an intermediate sloping beach dominated by incident wave energy. One or two offshore sand bars generally dominate the offshore bathymetry. Beach slopes typically range from 0.08 to 0.05 on the foreshore. Tide range is ~1 m.

Wave data for this period were obtained from an array of wave gauges located in 8 m water depth, slightly northeast of the FRF pier. Data on incident frequency, wave height, and wave angle were computed as means over 3-hour sampling periods. Tide data were available from the National Oceanic and Atmospheric Administration (NOAA) tide gauge located at the end of the pier. Daily bathymetric surveys were performed by the Coastal Research Amphibious Buggy (CRAB) along 18 cross-shore lines.

4.1. Sampling Design

Video data were collected hourly using two of five cameras positioned on a tower 43 m above sea level. The pixel sensor spacing of the sampling array (2.5 m) was selected to maximize the coherence between adjacent sensor locations while still allowing enough distance between the sensors for the identification of a statistically significant phase lag [*Lippmann and Holman,* 1991].

The pixel sampling array (Figure 4) was designed to cover the full extent of the main experiment region and spanned the view of two cameras. The 18 cross-shore lines each consist of 160 locations extending 400 m offshore from the shoreline (located at ~100 m). The longshore location y_i of the cross-shore lines was chosen to correspond with the locations of the daily CRAB surveys. Not all of the cross-shore lines contain 160 pixels because in some locations the lines extend outside of the field of view of the camera. Eight longshore-oriented lines are spaced 25 m in the cross-shore x_i. Individual pixel spacing for each point in the array is 2.5 m. Vertical locations z_i of the pixels were chosen as the predicted tidal elevation at midrun.

Using the known geometry of the image, the list of sampling locations (x_i, y_i, z_i) was converted to a corresponding list of pixel coordinates (Ui, Vi) [*Holland et al.,* 1997]. Timestacks of pixel intensity were then collected hourly at each point in the array at a rate of 2 Hz for 17 min.

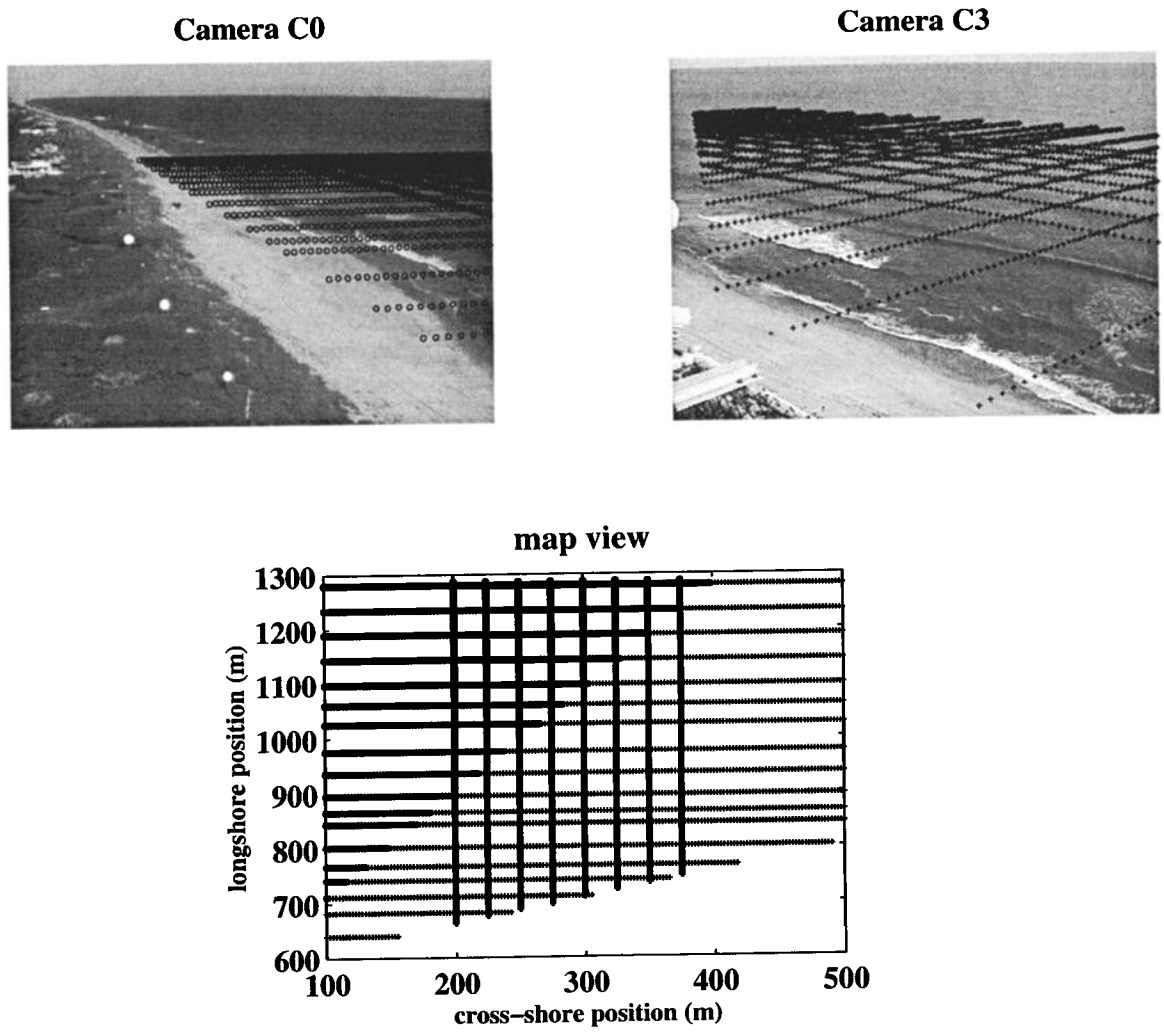

Figure 4. Pixel array for the SandyDuck experiment. The array covers the field of view from camera C0 (top left) and camera C3 (top right). When viewed as a map (bottom), the full extent of the array is shown to cover 400 m in the cross-shore and 700 m in the longshore.

A representative timestack of data collected during low wave conditions is shown in Figure 2. Bright regions, for example, around $x = 100$ m, are generally associated with white foam that results as waves break at the shoreline or over an underlying topographic high [*Lippmann and Holman,* 1989]. The diagonal traces of the wave crests define the shoreward progression of the waves. The CEOF analysis is used to extract phase speed and ultimately, water depth from these intensity data.

4.2. Results of Video Technique

To illustrate the details of the technique, we will use data collected on October 14, 1997, at 0700 LT (local time, Eastern Standard Time) along the cross-shore line located at $y = 801.8$ m (Figure 4). On this day the significant wave height measured in 8 m water depth was 0.58 m, the peak wave period was 10.7 s, and the wave approach was from the southeast, -14° from normal. Time exposure images showed mild wave breaking over a shallow terrace located 50 m offshore (approximately $x = 150$ m). The slope of the beach was ~0.035 in the inner surf zone.

Spectra were calculated using 42 degrees of freedom and a bandwidth of 0.0205 s^{-1} at each cross-shore position to identify the incident wave frequency. An average spectrum was calculated from the intensity spectra at all cross-shore sensor locations, and a peak frequency of 0.128 s^{-1} was calculated using (11).

A frequency-space plot showing the variability of the wave spectral density at each cross-shore location (Figure 5a) can be used to identify areas where the wave signal is best observed in the video data. The spectral peak is most clearly defined seaward of $x = 150$ m, before waves begin to break in shallower water. The absence of a spectral peak at some locations around the breakpoint indicates that the signal to noise ratio of the incident waves is not as strong in this region.

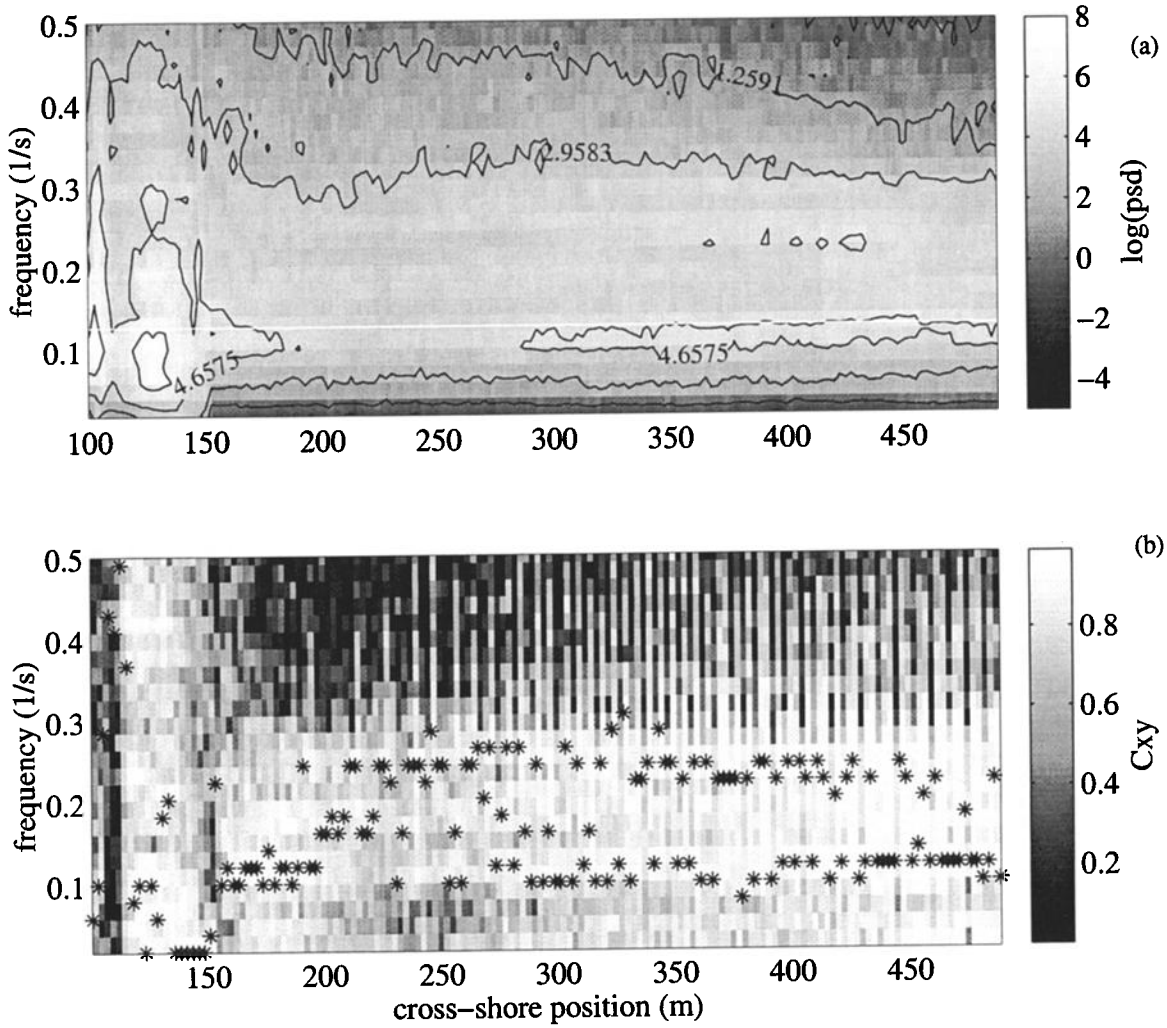

Figure 5. (a) Frequency-space spectra of intensity data and (b) frequency-space coherence between adjacent pixel sensors from October 14, 1997 at 0700 LT. Spectra are calculated with 42 degrees of freedom and a bandwidth of 0.0205 s^{-1} at each cross-shore position. The peak in the spectra is located at 0.128 s^{-1}. The offshore wave frequency as measured by the 8-m array at the Field Research Facility (FRF) is 0.933 s^{-1}. Solid stars indicate the frequency of maximum coherence. The 95% confidence interval is 0.14 s^{-1}. The coherence minimum near $x = 150$ m results from the intermittent occurrence of breaking (mixing two distinct modulation transfer function (MTF) phases).

Cross spectra were computed between each pair of adjacent sensors. The coherence between each pair (Figure 5b) reveals the areas where incident wave progression is best detected by the pixel sensors. High coherence is found in most regions of the profile at the incident frequency and at the first harmonic. Areas of low coherence throughout the incident band will likely correspond to regions of poor performance of the video-based technique.

The results of the CEOF analysis are presented in Figure 6. The cross-shore extent of Figure 6 is shorter than the cross-shore arrays because of spatial smoothing of phase after the CEOF was computed. The amplitude plot (Figure 6a) shows that the first EOF explains ~90% of the variance seaward of $x = 200$ m. In these areas of high EOF amplitude, a clear phase ramp (Figure 6b) is present, indicating the shoreward progression of waves. From the slope of the phase ramp the cross-shore wave number (Figure 6c) is calculated using (20). In other regions of low amplitude, reliable depth estimates are not expected.

Estimated wave angle and water depths for October 14, 1997, at 0700 LT are presented in Figure 7. The estimated wave angle presented in Figure 7a is generally consistent with that measured in 8 m water depth ($\alpha \sim -14°$). In Figure 7b, estimated water depths calculated using (10) are compared to the CRAB profile for this day. The rms difference error between the estimated and surveyed depths is 0.32 m over locations where the CEOF amplitudes are >0.60. For this run we expected

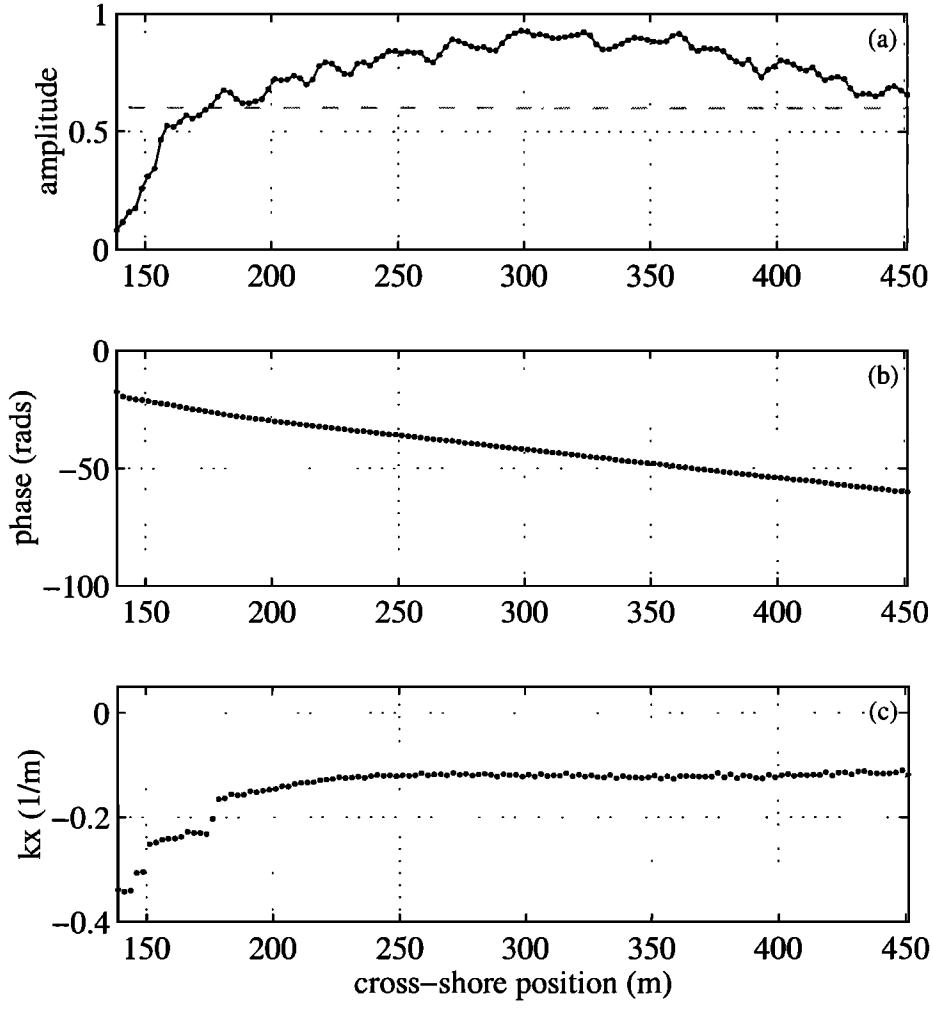

Figure 6. Complex empirical orthogonal function (CEOF) results for October 14, 1997, at 0700 LT. (a) Amplitude, (b) phase, and (c) cross-shore wavenumber are shown as a function of cross-shore position. High amplitudes across most of the profile indicate that the first EOF explains a significant amount of variance in this region. Cross-shore wavenumber is calculated from the slope of the phase ramp.

accurate results because the low-amplitude, long-period waves made the wave crests easy to identify. Errors around $x = 175$ m and over the bar may be associated with either of two mechanisms associated with the onset of breaking: nonlinear evolution of the wave field and/or the existence of strong spatial gradients in the MTF. Both mechanisms are explained below.

In the area of the profile associated with the onset of breaking, waves evolve from a sinusoid to a steep and peaky form as they begin to shoal and break. Just before breaking, the peaky crests created by the harmonics of the fundamental frequency shift forward [*Elgar and Guza,* 1985; *Flick et al.,* 1981]. Seaward of the breakpoint the MTF is dependent on sea surface slope variations associated with the wave field. Since slope increases with frequency, these higher harmonics can dominate the visual signature (an observer sees the steep front face of the wave), and their forward shift will cause video measurements of phase speed to be anomalously high.

At the breakpoint the mechanism of sea surface radiance changes from the specular reflection of nonbreaking waves to a diffuse scattering signature in the surf zone. While both are coherent and spatially stable in phase, they are distinctly different and individual to the signature of the wave in each region. In the region of the profile marked by a mixture of breaking and nonbreaking waves, the mix of the two different MTF phases will severely degrade the coherence between adjacent sensors.

The region of the breakpoint is associated with a peak in a plot of mean intensity at $x = 150$ m (over a terrace feature). In this region the low amplitudes from the first mode of the CEOF and resulting poor depth estimates may be attributed to the strong shift in the MTF.

4.3. Water Depth Analysis

The accuracy of the technique was tested using hourly data collected over a 30-day period from October 1 to October 30, 1997. Water depths were calculated at each

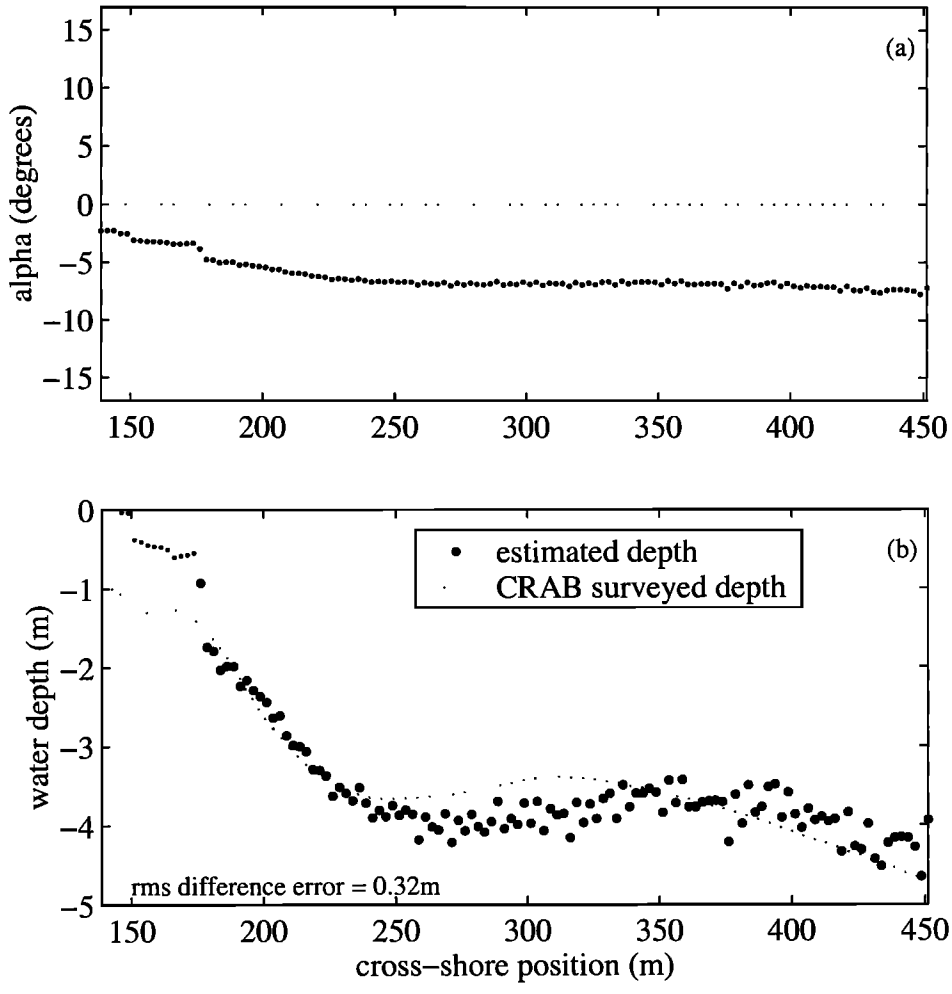

Figure 7. (a) Wave angle and (b) water depth estimates for October 14, 1997, at 0700 LT. The wave angle is shown to refract toward shore normal as it shoals. The estimates are generally consistent with the wave angle measured at the 8 m array (~14°). Estimated water depths are shown to be consistent with the Coastal Research Amphibious Buggy (CRAB) surveyed profile (rms error = 0.32 m) in areas of the profile where CEOF amplitudes are >0.60 (larger symbols).

position along the 18 cross-shore lines for every timestack. For each of the 300 timestacks collected over the month period, depth estimates were calculated at each cross-shore position. This resulted in over 710,000 independent estimates of water depth across the entire array.

Before examining the statistics of the results, the data were screened based on three criteria that eliminated physically impossible or statistically unstable estimates:

1. Only onshore phase speed would be used in the estimation of water depth. In the coordinate system defined for Duck a wave moving toward the shore would be moving in a negative x direction corresponding to a negative wavenumber. We limited our depth estimates to those instances where the wavenumbers calculated from the CEOF were negative.

2. Wavelengths were only considered if they were <0.9 times the theoretical deep water wavelength (see earlier discussion on the sensitivity of the dispersion relationship).

3. Estimated depths were only considered for which the corresponding amplitude from the CEOF was >0.60.

Screening the initial results using the above criteria eliminated ~55% of the estimates from the data set (still leaving over 319,000 estimates).

4.3.1. Definitions of statistics describing performance. Hourly data from each day were used to obtain a daily estimate for the bathymetry at each line in the array (Figure 8); therefore, at each cross-shore position, from a few to as many as 10 tide-corrected depths $h_i(x)$ were estimated. A great amount of variability was observed between the hourly estimates as the stages of the tide shifted throughout the day. We investigated the relative performance of four statistics (the arithmetic and geometric means, the mode, and median) as possible methods to determine a best single estimated depth $\hat{h}(x)$ from the set of individual estimates collected over the day [*Bendat and Piersol*, 1986].

Each estimator has a confidence interval based on the variance of the data around the estimate. On the basis

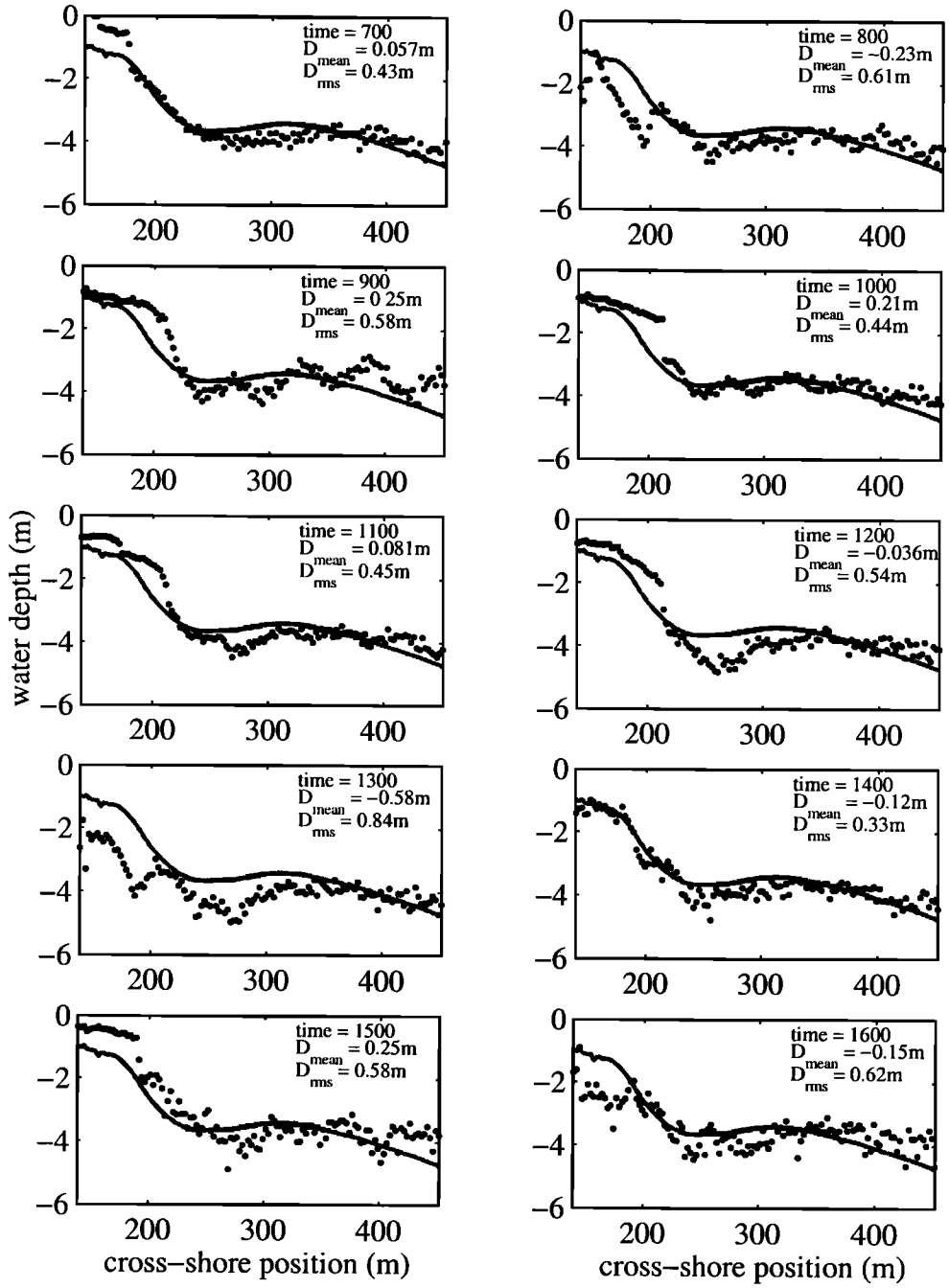

Figure 8. Estimated profiles along y = 801.8 m for October 14, 1997, from 0700 to 1600 LT. The 10 profiles show how the estimates along one line vary through the day as tide level and lighting conditions change.

of the central limit theorem a 95% confidence interval $E(x)$ associated with the arithmetic mean can be defined as

$$E(x) = \frac{1.96 s(x)}{\sqrt{N}}, \tag{23}$$

where s is the standard deviation of the estimates and N is the number of points. While this measure of error is not strictly valid for the other statistics, we will still use it as a useful proxy for an error bar.

Once the average estimated profile had been determined and confidence intervals established, bulk performance statistics on the estimated profile were calculated for each of the four measures (mean, geometric mean, median, and mode).

Performance was measured in terms of actual difference errors $D(x)$,

$$D(x) = \hat{h}(x) - h_t(x), \tag{24}$$

and relative errors $R(x)$,

$$R(x) = \frac{\left(\hat{h}(x) - h_t(x)\right)}{h_t(x)}, \tag{25}$$

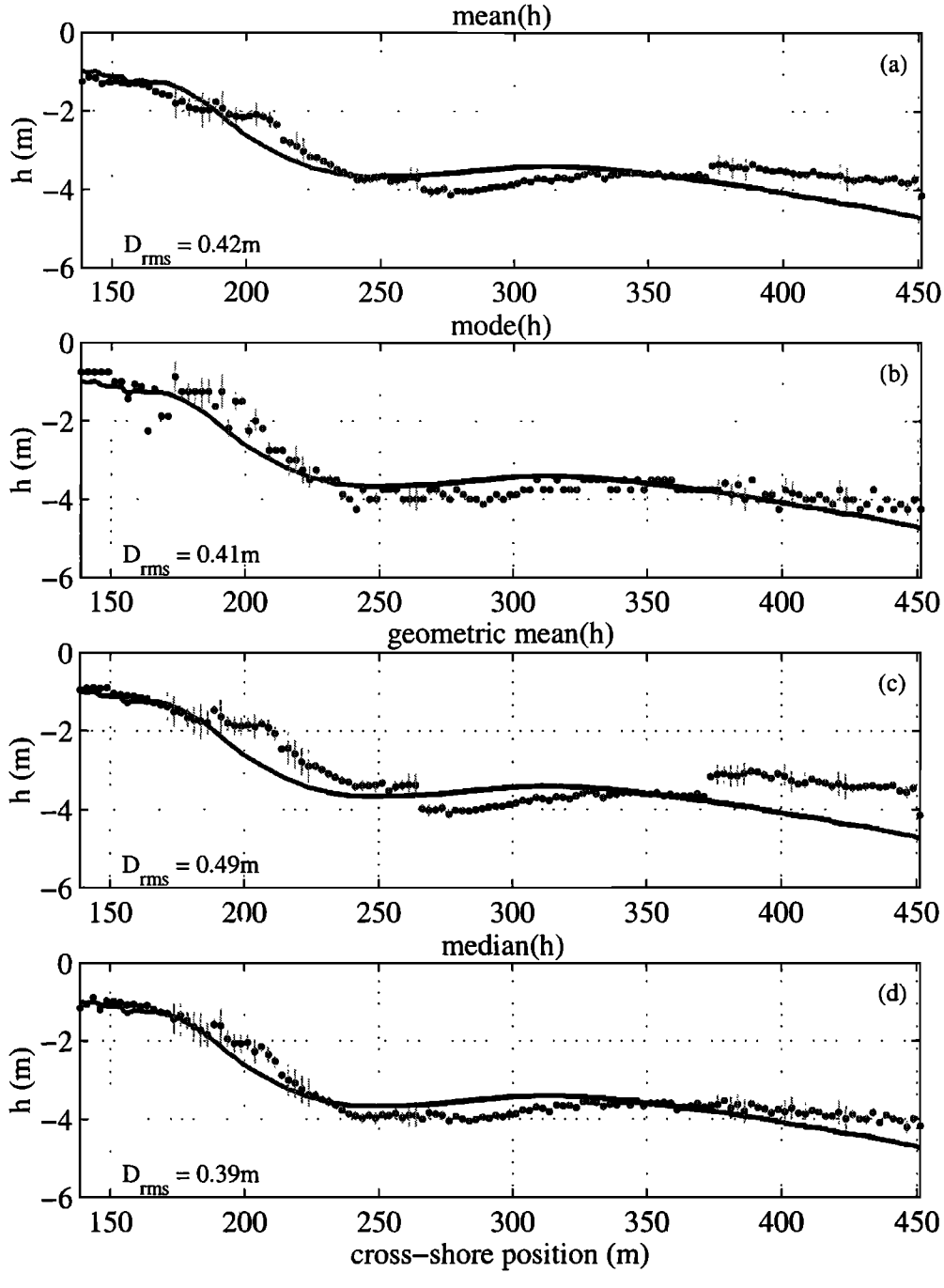

Figure 9. Estimated profile at Duck, North Carolina, for October 14, 1997, at $y = 801.8$ m. The four profiles represent 10-hour averaged profiles calculated as the (a) mean, (b) mode, (c) geometric mean, and (d) median of all the estimates at cross-shore position x for that day. Error bars on depth represent the 95% confidence interval based on the standard deviation of the estimates about the mean. The estimated profile determined from the median value of depth at each location is the most accurate (rms error is 0.39 m) and spatially stable of the four.

where $h_t(x)$ is the true water depth. Note that a negative value of D indicates an overestimate as water depths in this study are defined to be negative. A mean $D(x)$ and $R(x)$ can be calculated across the entire profile for each daily estimate by

$$\bar{D} = \frac{1}{N_x}\sum_{i=1}^{N_x} D(x_i), \tag{26}$$

$$\bar{R} = \frac{1}{N_x}\sum_{i=1}^{N_x} R(x_i), \tag{27}$$

where N_x is the number of cross-shore locations. The root-mean-square (rms) error of the differences, calculated as

$$D_{\mathrm{rms}} = \sqrt{\frac{1}{N}\sum_{i=1}^{N} D(x_i)^2}, \tag{28}$$

is used to measure the scatter of mean differences. A rms relative error is calculated across the entire profile by

$$R_{\text{rms}} = \sqrt{\frac{1}{N}\sum_{i=1}^{N} R(x_i)^2}\,. \tag{29}$$

4.3.2. Evaluation of depth estimators. Figure 9 presents an estimated profile based on the four measures for October 14, 1997. Panels show estimates derived, top to bottom, from the arithmetic mean, the mode (bin width is 0.25 m), the geometric mean, and the median. A disadvantage of the arithmetic and geometric means of the estimated depths is that they can be influenced by a few deep outliers, resulting in a bias to deeper estimates. Mode and median estimates are insensitive to outliers. In this example, the rms difference error D_{rms} for the median estimate is 0.39 m, while D_{rms} for the other three methods ranges between 0.41 and 0.49 m. The median value more accurately estimates the true water depth and presents a better defined (generally smoother) profile. In areas with large error bars the median value provided the most robust estimate of the true water depth. These results were confirmed by statistics from the entire month of data. Thus, for the remainder of the paper, only estimates based on the median over each day will be considered.

To establish general error statistics for this technique, performance was examined over three adjacent cross-shore profiles, located close to the camera. For the profile line at y = 865 m, the time averaged difference error (or mean bias) $\bar{D}$ between the median depth and the true depth was -0.26 m (D_{rms} = 0.91 m) over the 30-day period. The mean (rms) relative error $\bar{R}$ for this profile was 0.11 (0.34), indicating that the estimated water depths were generally 11% (34%) deeper than the actual surveyed water depths. Similar statistics were calculated for the profiles measured along either side of y = 865 m (see Table 1). At y = 801.8 m the mean difference error $\bar{D}$ was -0.29 m (D_{rms} = 0.83 m), and $\bar{R}$ was also 0.11 (R_{rms} = 0.30). Along the profile at y = 935 m, $\bar{D}$ was -0.50 m (D_{rms} = 0.99 m), and $\bar{R}$ was 0.17 (R_{rms} = 0.38). On the basis of these analyses the error on individual video-based depth estimates calculated as the median depth at each cross-shore location is 91 cm (including noise and bias). Averaging along the profile can help to eliminate noise, and the error can be reduced to a minimum value of 35 cm (mean bias).

4.3.3. Algorithm performance. In order to investigate the details of when the technique is most accurate and under what conditions the technique may fail, the difference error and the variance associated with each estimate were examined for dependencies on environmental conditions. First, the accuracy of the technique was examined relative to cross-shore position to determine if the technique works better in one region of the profile over another. The mean D_{rms} of the estimates at each cross-shore position is presented in Figure 10a. The greatest amount of variability in the depth estimates is seen between the shoreline and x = 200 m. This region generally marks the location of a terrace or inner sand bar where wave breaking and reformation tend to lower the coherence. In Figure 10b the difference errors are compared to the actual water depths. In shallow water the technique tended to overpredict the water depth, as indicated by the negative values of D (the mean bias $\bar{D}$ for depths shallower than -3 m is -0.63 m). This is likely associated with the slight increase of phase speed known to be due to finite amplitude waves. In deeper water, water depths were not as dramatically overpredicted, as seen by the cluster of difference errors around zero located in regions deeper than h = -4 m. The mean bias in this region is -0.20 m. The large cluster of errors at h = -3.5 m corresponds to the wide region of near-constant depth over a subtle outer bar that existed during this period (Figure 10b). Interestingly, the bulk performance statistics noted in section 4.3.2 appear to be a worst case scenario for the technique. If the region of high variance around 200 m is omitted, the mean bias $\bar{D}$ becomes -0.28 m.

Occasionally, depths appear to be overestimated in the region associated with the onset of breaking, a consequence of the spatial shift in the MTF phase as the wave changes form from sinusoid to sawtooth-like. To investigate this phenomenon and the effects on the estimated water depths, difference errors and estimate variance were plotted against the gradient in mean intensity between adjacent cross-shore positions, $d\bar{I}/dx$ (not shown). No significant relationship was found, perhaps because most of the bad data would have been previously filtered out by the significance test (CEOF amplitude >0.6).

It was also determined that the larger errors occur during large wave conditions. Figure 11 presents a comparison of the daily mean difference error over the month along the profile at y = 865 m and the offshore

Table 1. Accuracy of Depth Estimates Along Three Cross-Shore Profile Lines

Longshore position, m	Mean Difference Error $\bar{D}$, m	RMS Difference Error D_{rms}, m	Mean Relative Error $\bar{D}$	RMS Relative Error R_{rms}
801.8	-0.29	0.83	0.11	0.30
865	-0.26	0.91	0.11	0.34
935	-0.50	0.99	0.17	0.38

Table 2. Accuracy of Depth Estimates Over the Three Profiles at x = 801.8, 865, and 935 m.

	Mean Difference Error $\bar{D}$, m	RMS Difference Error D_{rms}, m	Mean Relative Error $\bar{R}$	RMS Relative Error R_{rms}
All data	-0.35	0.91	0.13	0.34
$H \leq 1$ m	-0.12	0.71	0.06	0.29
$h < -3.5$ m	-0.20	0.75	0.05	0.20

Statistics are calculated across the entire profile for all data, for data collected during low wave conditions ($H \leq 1$ m, entire profile), and for data collected offshore of the sand bar (prior to breaking at h = -3.5 m, all wave conditions).

wave height. Larger errors are associated with wave heights >1 m. The errors may be due to the larger-amplitude waves breaking over the bar, finite amplitude effectively increasing wave phase speed, or poor coherence of the stormy, short-crested seas that often accompany larger east coast waves. The mean bias $\bar{D}$ across the entire profile for times when the wave height was <1 m (60% of the data runs) was only -0.12 m, and the percent error, $\bar{R}\times$ 100, was 6%. Table 2 summarizes the accuracy of the technique over all data and also for those conditions where the technique is believed to be more robust.

5. Discussion

The video-based technique was shown to be most accurate when the median of a suite of estimates at one particular cross-shore position was chosen as a representative single water depth. On the bases of results of the analysis of 30 days of data from Duck, North

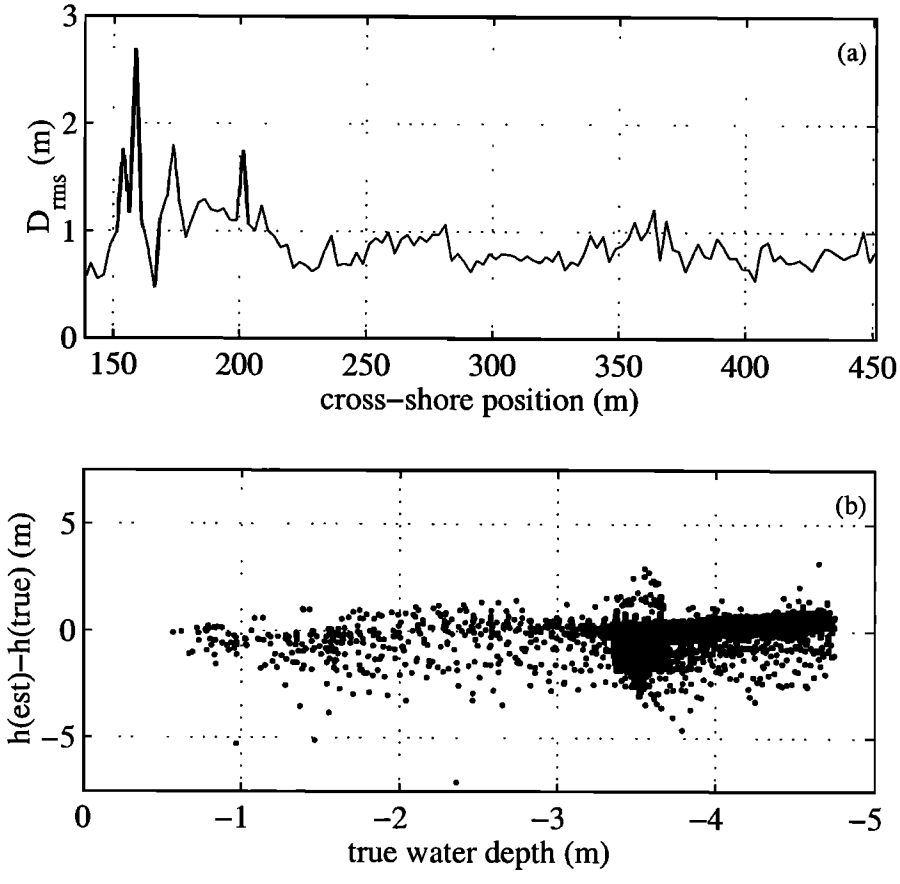

Figure 10. (a) Rms difference error D_{rms} at each cross-shore position and (b) estimated depth error compared to true water depth for October 1997. The region around x = 200 m is generally associated with the slope break before the shoreface where waves will preferentially break, causing larger errors. Waves will then break again along the shoreline near x = 150 m. Estimates are generally overpredicted in shallow water (negative difference errors to the left (Figure 10b)) and underpredicted in deeper water (positive difference errors to the right (Figure 10b)). Large errors in water depths between -3.25 and -3.5 m may be attributed to wave breaking in this region.

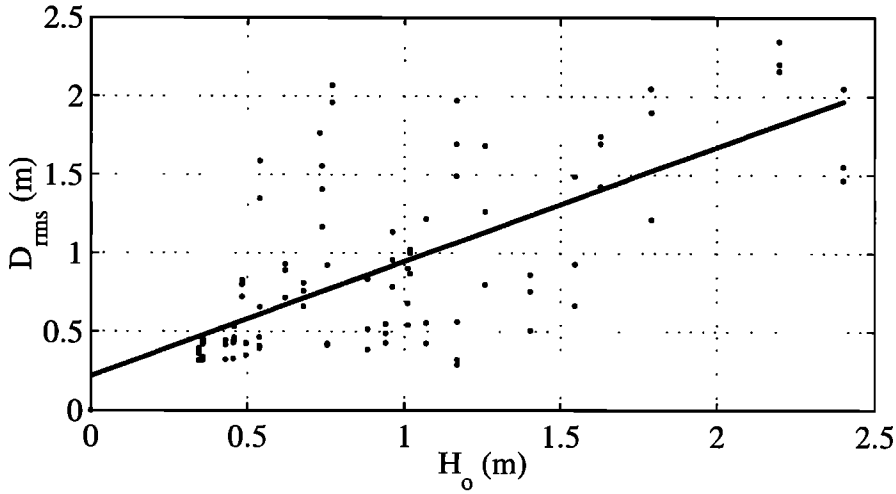

Figure 11. Rms difference error D_{rms} versus wave height. Larger errors are observed as wave heights increase (regression model skill is 0.48). This may be due to wave breaking over the bar or broad-banded spectra generally associated with large east coast storm waves.

Carolina, the mean (rms) difference error for the video technique was -0.35 m (0.91 m). The mean (rms) relative error was 0.13 (0.34), indicating on average a 13% (34%) overestimation of water depth.

Accuracy of the technique depends on the signal to noise ratio (SNR) of the wave signal compared to background optical "noise," a function of the environmental conditions during the time of sampling. Rain, fog, and poor lighting conditions all obscure the visual signature of the waves either directly or by reducing or eliminating the sky gradient. Sun glare can add large amounts of speckle noise. During SandyDuck, individual depth estimates were averaged over the course of 1 day (through a wide range of viewing conditions) to reduce the noise associated with these problems.

Performance of video imaging of waves is expected to degrade with increased distance from the camera and with viewing angle. During the SandyDuck experiment the accuracy of the technique was found to be greatest along lines closest to the camera (located at 550 m in the FRF coordinate system). The rms difference error D_{rms} along each cross-shore line is shown to increase with increasing distance (and angle) from the camera (Figure 12). It might be suspected that this is simply a consequence of the decrease of pixel resolution with distance, but for the ranges considered in this study, pixel footprints (0.35–0.75 m/pixel) are always much smaller than incident wave wavelengths and so are not as limiting. More important are variations due to viewing geometry on the radiance received from the sea surface.

A full study of the physics of optical imaging of an ocean wave field would be well beyond the scope of this paper; however, some estimates can be made. The dominant influence on radiance can be taken to be the reflection coefficient of the ocean surface since upwelled light from the ocean interior is much darker than reflected skylight. The reflection coefficient, in turn, depends only on the angle θ between the local sea surface normal and the direction of view. As the look direction changes with respect to the direction of wave approach, the magnitude of θ variations due to the presence of waves changes. At typical ranges for this site, simulations show a 50% reduction in signal strength (factor of 4 decrease in signal variance) when looking along wave crests compared to looking directly into the oncoming crests. Similarly, for normally incident waves, the signal strength at 1 km along the beach from the camera is ~10-20% the strength of the signal seen directly offshore of the camera location.

Certain wave conditions are more advantageous for use with the video technique. A clean narrow-banded swell increases the SNR, making the task of identifying a peak frequency rather straight forward. A broad-banded or directionally spread spectrum, containing many different wave frequencies and wavelengths, is likely to degrade the Fourier analyses and make it difficult to resolve the frequency of interest. No rigorous theory has been developed to quantify the relationship between wave conditions and error; however, it was clearly observed at SandyDuck during a northeasterly storm from October 18 to 22 when wave heights reached 3.5 m. Accurate profiles could not be estimated immediately before and during the storm. Generally, during periods of increasing wave height associated with storms, the spectrum is broad-banded, and an incident frequency is hard to identify. As waves dispersed and amplitudes decreased after the storm had passed, the spectra became narrow-banded, and reliable depth estimates were obtained. Estimate made during periods of low-amplitude swell are also less like to be contaminated by finite-amplitude dispersion effects.

Errors may also be introduced as a result of the de-

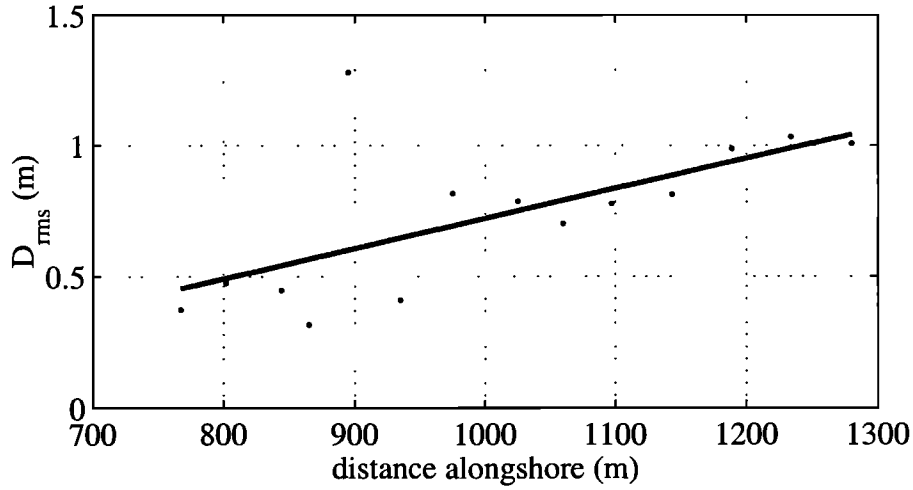

Figure 12. Rms difference error D_{rms} along each cross-shore line versus distance from the camera. Errors increase with increasing distance from the camera and with increased viewing angle (regression model skill is 0.42).

tails of the analysis approach. The CEOF analysis is a robust method for determining the phase relationship across a spatial array; however, it may be sensitive to array length and sensor spacing resulting in regions of low coherence. *Merrifield and Guza* [1990] showed that the performance of a CEOF analysis from a spatial array depends on the wavenumber bandwidth times the array length. Performance degrades at large values, especially toward the ends of the array. Better performance was achieved for broad wavenumber bands using shorter subsection and thereby retaining the coherence at the ends of the array. Alternately, to obtain the most accurate results using longer spatial arrays, a narrow wavenumber band should be investigated. This indicates that a piecewise approach to the CEOF may be a viable alternative. By separating the array into smaller areas of interest, perhaps greater coherence can be achieved between sensors, and the percentage of the variance explained by the first mode of the EOF will increase, thus increasing the accuracy of the estimates.

Finally, errors may arise due to inaccuracies in the linear dispersion relationship. Phase speeds in the nearshore can be affected by many physical processes, such as surface drift currents, mean flows, and rip currents [*Plant and Wright,* 1980], the directional spread of wave energy [*Huang and Tung,* 1977], the presence of shorter waves traveling on low-frequency long waves [*Phillips,* 1981], and finite-amplitude dispersion [*Dean and Dalrymple,* 1991].

Estimated phase speeds may also be compared to those predicted by solitary theory, which accounts for the effects of finite-amplitude dispersion. While linear wave theory is generally accurate within a first-order approximation, some data have suggested that solitary theory may be a more appropriate and accurate estimator of phase speed at shallower locations within the surf zone [*Thornton and Guza,* 1982]. The phase speed of a wave based on solitary theory is

$$c_s = \sqrt{g(h+H)}\,, \tag{30}$$

where H is the height of the wave [*Komar,* 1976]. The potential errors associated with inferring water depths from linear theory (h_l) rather than solitary theory (h_s) can be calculated from (6) and (30) as

$$\frac{h_1}{h_2} = \frac{\left(\frac{c^2}{g}\right)}{\left(\frac{c_s^2}{g(1+H/h)}\right)} = \frac{\left(\frac{c^2}{g}\right)}{\left(\frac{c_s^2}{1.42g}\right)} = 1.42\,, \tag{31}$$

where the ratio H/h is taken to be 0.42 in the saturated surf zone [*Thornton and Guza,* 1982]. Thus overestimates of up to 42% may be associated with finite-amplitude dispersion. *Grilli* [1998] found that depth inversion techniques based solely on linear theory may lead to errors of 50-70%. Preferential selection of low-amplitude wave conditions (perhaps determined by a proxy for wave height such as total wave breaking signature from time exposure images) can allow avoidance of this problem.

6. Conclusion

A new technique has been developed for the estimation of bathymetry from remote video measurements of wave phase progression. While not a new idea per se, the technique is an advance because it involves careful time series analysis of 17-min time series of pixel intensity, collected over a dense array of cross-shore and longshore locations. Wavenumber estimation is based on the phase structure of the first EOF of the cross-spectral matrix over the incident band.

The accuracy of the video technique was tested using data from the SandyDuck experiment conducted in Duck, North Carolina, from October 1997. Hourly (daytime) estimates were made with a cross-shore spacing of 2.5 m along 18 cross-shore transects for 30 days (710,000 individual estimates). Daily averaged profiles were determined using the arithmetic mean, geometric mean, median, and mode of the hourly estimates at each x position with a confidence interval computed using the standard deviation. Results based on the median provided the lowest rms error and best spatial stability.

The bias for data collected along three lines located near the camera was -0.35 m (mean percent error of 13%) with a rms error of 0.91 m. The region in the vicinity of the breakpoint is not well sampled owing to both the presence of a large spatial gradient in phase of incident wave harmonics (a rapidly changing wave shape) and the poor coherence associated with the mixed optical signatures of breaking versus nonbreaking waves. Collection of estimates over varying tide levels offers a solution to this problem. Data with low coherence (as measured by the amplitude of the first complex EOF in the incident band) and data for which the local estimated wavelength is >90% of the deep water wavelength (errors in depth estimates are >4 times errors in wavelength) are automatically omitted from analysis.

Selection of appropriate subregions and wave conditions allows considerable improvement on the above statistics. For the month-long test discussed here, poor performance was concentrated on a relatively narrow region on the seaward flank of a sand bar. Offshore of this region (deeper than h = -3.5 m) the mean bias was -0.20 m ($D_{\mathrm{rms}} = 0.75$ m), and the percent error was 5% ($R_{\mathrm{rms}} = 20\%$). The technique was also more accurate during periods of low-amplitude waves (H <=1 m). The mean bias across the entire profile during times of low waves was -0.12 m ($D_{\mathrm{rms}} = 0.71$ m), and the percent error was 6% ($R_{\mathrm{rms}} = 29\%$).

While not of comparable accuracy to conventional survey techniques, the video method is inexpensive, features simple logistics that are immune to damage from bad weather, and can be sampled frequently for extended periods of time with no additional costs (beyond automated analysis). Thus errors of individual analyses can be reduced through extensive averaging, and long time series of nearshore evolution can become available at low cost.

Acknowledgments. The authors wish to thank John Stanley for his extensive help with all aspects of the video data collection, storage, and processing. The dedicated staff at the FRF provided a wealth of bathymetric and wave data that were used as ground truth in this study. Drew Toland provided valuable input on the sensitivity of results to viewing geometry. We would like to thank the Office of Naval Research (N00014-96-1-0237) for support of this project.

References

Aarninkhof, S., and R.A. Holman, Monitoring the nearshore with video, *Backscatter, 10(2),* 8–11, 1999.

Bell, P.S., Shallow water bathymetry derived from an analysis of X-band marine radar images of waves, *Coastal Eng., 37,* 513–527, 1999.

Bendat, J.S., and A.G. Piersol, it Random Data: Analysis and Measurement Techniques, 566 pp., Wiley Intersci., New York, 1986.

Bowen, A.J., and D.L. Inman, Edge waves and crescentic bars, *J. Geophys. Res., 76*(36), 8662–8671, 1971.

Bryan, K.R., and A.J. Bowen, Edge wave trapping and amplification on barred beaches, *J. Geophys. Res., 101*(C3), 6543–6552, 1996.

Dean, R.G., and R.A. Dalrymple, *Water Wave Mechanics for Engineers and Scientists,* 353 pp., World Sci., River Edge, N.J., 1991.

Elgar, S., and R.T. Guza, Observations of bispectra of shoaling surface gravity waves, *J. Fluid Mech., 161,* 425–448, 1985.

Flick, R.E., R.T. Guza, and D.L. Inman, Elevation and velocity measurements of laboratory shoaling waves, *J. Geophys. Res., 86*(C5), 4149–4160, 1981.

Fuchs, R.A., Depth determination on beaches by wave velocity methods, *Rep. 74-1,* Univ. of Calif., Berkeley, 1953.

Gonzales, R.C., and R.E. Woods, *Digital Image Processing,* 716 pp., Addison-Wesley-Longman, Reading, Mass., 1992.

Greidanus, H., The use of radar for bathymetry in shallow seas, *Hydrographic J., 83,* 13–18, 1997.

Grilli, S.T., Depth inversion in shallow water based on nonlinear properties of shoaling periodic waves, *Coastal Eng., 35,* 185–209, 1998.

Holland, K.T., and R.A. Holman, Wavenumber-frequency structure of infragravity swash motions, *J. Geophys. Res., 106*(C6), 13,479–13,488, 1999.

Holland, K.T., B. Raubenheimer, R.T. Guza, and R.A. Holman, Runup kinematics on a natural beach, *J. Geophys. Res., 100*(C3), 4985–4993, 1995.

Holland, K.T., R.A. Holman, T.C. Lippmann, J. Stanley, and N. Plant, Practical use of video imagery in nearshore oceanographic field studies, *IEEE J. Oceanic Eng., 22*(1), 81–92, 1997.

Holman, R.A., and A.J. Bowen, Edge waves on complex beach profiles, *J. Geophys. Res., 84*(C10), 6339–6346, 1979.

Huang, N.E., and C.C. Tung, The influence of the directional energy distibution on the nonlinear dispersion relation in a random gravity wave field, *J. Phys. Oceanogr., 7,* 403–414, 1977.

Johnson, J.W., Progress report: Wave-velocity method of depth determination by aerial photographs, *Tech. Rep. 155-10,* Univ. of Calif., Berkeley, 1949.

Komar, P.D., *Beach Processes and Sedimentation,* 429 pp., Prentice-Hall, Englewood Cliffs, N. J., 1976.

Leu, L.G., Y.Y. Kuo, and C.T. Lui, Coastal bathymetry from the wave spectrum of SPOT images, *Coastal Eng. J., 41,* 21–41, 1999.

Lippmann, T.C., and R.A. Holman, Quantification of sand bar morphology: A video technique based on wave dissipation, *J. Geophys. Res., 94*(C1), 995–1011, 1989.

Lippmann, T.C., and R.A. Holman, The spatial and temporal variability of sand bar morphology, *J. Geophys. Res., 95*(C7), 11,575–11,590, 1990.

Lippmann, T.C., and R.A. Holman, Phase speed and angle of breaking waves measured with video techniques, in *Coastal Sediments, '91,* edited by N. Kraus, pp. 542–556, Am. Soc. of Civ. Eng., New York, 1991.

Longuet-Higgins, M.S., Longshore currents generated by obliquely incident waves, 1, *J. Geophys. Res., 75,* 6778–6789, 1970.

Lynch, D.K., and W. Livingston, *Color and Light in Nature,* 245 pp., Cambridge Univ. Press, New York, 1995.

Merrifield, M.A., and R.T. Guza, Detecting propagating sig-

nals with complex empirical orthogonal functions: A cautionary note, *J. Phys. Oceanogr., 20,* 1628–1633, 1990.

Phillips, O.M., The dispersion of short wavelets in the presence of a dominant long wave, *J. Fluid Mech., 107,* 465–485, 1981.

Plant, N.G., and R.A. Holman, Intertidal beach profile estimation using video images, *Mar. Geol., 140,* 1–24, 1997.

Plant, W.J., and J.W. Wright, Phase speeds of upwind and downwind traveling short gravity waves, *J. Geophys. Res., 85*(C6), 3304–3310, 1980.

Sallenger, A.H., Jr., and P.A. Howd, Nearshore bars and the break-point hypothesis, *Coastal Eng., 12,* 301–313, 1989.

Shepard, F.P., Longshore bars and troughs, Beach Erosion Board Tech. Memo 15, U.S. Army Corps of Eng., Washington, D.C., 1950.

Suhayda, I.N., and N.R. Pettigrew, Observations of wave height and wave celerity in the surf zone, *J. Geophys. Res., 82*(9), 1419–1424, 1977.

Thornton, E.B., and R.T. Guza, Energy saturation and phase speeds measured on a natural beach, *J. Geophys. Res., 87*(C12), 9499–9508, 1982.

Wallace, J.M., and R.E. Dickinson, Empirical orthogonal representation of time series in the frequency domain, part I; Theoretical considerations, *J. Appl. Meteorol., 11*(6), 887–892, 1972.

Wiegel, R.L., and R.A. Fuchs, Wave velocity method of depth determination for non-uniform short-crested wave systems by aerial photography, *Rep. 74-9,* Univ. of Calif., Berkeley, 1953.

Williams, W.W., The determination of gradients of enemy-held beaches, *Geogr. J., 107,* 76-93, July 1946.

Wright, L.D., and A.D. Short, Morphodynamic variability of surf zones and beaches: A synthesis, *Mar. Geol., 56,* 93–118, 1984.

R.A. Holman, College of Oceanic and Atmospheric Sciences, Oregon State University, Corvallis, OR 97331. (holman@oce.orst.edu)

H.F. Stockdon, Center for Coastal Geology, U.S. Geological Survey, 600 Fourth Street South, St. Petersburg, FL 33701. (hstockdo@usgs.gov)

(Received November 1, 1999; revised April 25, 2000; accepted May 25, 2000.)